NASA/TM-20220001759

Prediction of Turbulent Diffusing Flows Using FUN3D

David J. Friedlander, Julianne C. Dudek, and May-Fun Liou
Glenn Research Center, Cleveland, Ohio

February 2022

NASA STI Program . . . in Profile

Since its founding, NASA has been dedicated to the advancement of aeronautics and space science. The NASA Scientific and Technical Information (STI) Program plays a key part in helping NASA maintain this important role.

The NASA STI Program operates under the auspices of the Agency Chief Information Officer. It collects, organizes, provides for archiving, and disseminates NASA's STI. The NASA STI Program provides access to the NASA Technical Report Server—Registered (NTRS Reg) and NASA Technical Report Server—Public (NTRS) thus providing one of the largest collections of aeronautical and space science STI in the world. Results are published in both non-NASA channels and by NASA in the NASA STI Report Series, which includes the following report types:

- TECHNICAL PUBLICATION. Reports of completed research or a major significant phase of research that present the results of NASA programs and include extensive data or theoretical analysis. Includes compilations of significant scientific and technical data and information deemed to be of continuing reference value. NASA counter-part of peer-reviewed formal professional papers, but has less stringent limitations on manuscript length and extent of graphic presentations.

- TECHNICAL MEMORANDUM. Scientific and technical findings that are preliminary or of specialized interest, e.g., "quick-release" reports, working papers, and bibliographies that contain minimal annotation. Does not contain extensive analysis.

- CONTRACTOR REPORT. Scientific and technical findings by NASA-sponsored contractors and grantees.

- CONFERENCE PUBLICATION. Collected papers from scientific and technical conferences, symposia, seminars, or other meetings sponsored or co-sponsored by NASA.

- SPECIAL PUBLICATION. Scientific, technical, or historical information from NASA programs, projects, and missions, often concerned with subjects having substantial public interest.

- TECHNICAL TRANSLATION. English-language translations of foreign scientific and technical material pertinent to NASA's mission.

For more information about the NASA STI program, see the following:

- Access the NASA STI program home page at http://www.sti.nasa.gov

- E-mail your question to help@sti.nasa.gov

- Fax your question to the NASA STI Information Desk at 757-864-6500

- Telephone the NASA STI Information Desk at 757-864-9658

- Write to:
  NASA STI Program
  Mail Stop 148
  NASA Langley Research Center
  Hampton, VA 23681-2199

NASA/TM-20220001759

Prediction of Turbulent Diffusing Flows Using FUN3D

David J. Friedlander, Julianne C. Dudek, and May-Fun Liou
Glenn Research Center, Cleveland, Ohio

National Aeronautics and
Space Administration

Glenn Research Center
Cleveland, Ohio 44135

February 2022

Acknowledgments

The authors would like to thank the NASA Revolutionary Computational Aerosciences under the Transformational Tools and Technologies Project for funding and the NASA's High-End Computing Program for providing super-computing resources.

This work was sponsored by the
Transformative Aeronautics Concepts Program.

Level of Review: This material has been technically reviewed by technical management.

Available from

NASA STI Program
Mail Stop 148
NASA Langley Research Center
Hampton, VA 23681-2199

National Technical Information Service
5285 Port Royal Road
Springfield, VA 22161
703-605-6000

This report is available in electronic form at http://www.sti.nasa.gov/ and http://ntrs.nasa.gov/

Prediction of Turbulent Diffusing Flows Using FUN3D

David J. Friedlander, Julianne C. Dudek, and May-Fun Liou
National Aeronautics and Space Administration
Glenn Research Center
Cleveland, Ohio 44135

Abstract

The FUN3D code was used to perform Reynolds-averaged Navier-Stokes (RANS) simulations to compute subsonic flow in an S-duct diffuser and transonic flow in a two-dimensional diffuser using the Speziale-Sarkar-Gatski/Launder-Rodi-Reece (SSG/LRR) Reynolds stress model (RSM). For comparison purposes, additional simulations were run with the one-equation Spalart-Allmaras (SA) and the two-equation Menter Shear-Stress Transport (SST) turbulence models. Each model was run with and without the quadratic constitutive relation (QCR) for computing the turbulent stresses. It was shown that the simulations that utilized the RSM had better overall predictions of the diffusive flow fields compared to the simulations that utilized the one and two equation turbulence models.

Nomenclature

D	diameter
DPCP	inlet circumferential distortion
DPRP	inlet radial distortion
h	height
M	Mach number
MPR	multiple per revolution (number of equivalent low pressures regions)
N	grid complexity
p, p_0	static and total pressure
$p_{0,2}$ / $p_{0,\infty}$	inlet total pressure recovery
u	streamwise velocity
$u'v'$	Reynolds xy-component shear stress
x, y, z	Cartesian coordinates
y^+	nondimensional wall distance
μ	eddy viscosity

Subscripts

AIP	aerodynamic interface plane
H	hub
i	ring index
T	tip
t	turbulent
0	total condition
∞	freestream

1.0 Introduction

There is an interest within the aviation community to move in the direction of more certification by analysis (Refs. 1 and 2), with a motivation to reduce flight and wind tunnel testing requirements, which can be costly relative to numerical analysis. While some aircraft components are already certified by analysis (Ref. 3), other components, such as the propulsion system, are still years away (Ref. 4). The importance of accurately simulating the propulsion system was emphasized within the CFD 2030 Vision Study report as one of the proposed grand challenges (Ref. 4). In response to the report, the NASA Aeronautics Research Mission Directorate was tasked, and is currently looking into, developing state-of-the-art computational tools for simulating aerospace vehicles/components and accurately predicting their performance (Ref. 5). A subset of that research is exploring how to predict inlet performance using computational fluid dynamics (CFD), with a goal of developing a set of best practices for simulating inlet flows with CFD simulations ranging from Reynolds-averaged Navier-Stokes (RANS) to Large-Eddy Simulations (LES). This is partially motivated by the trend that future electric aircraft would like to take advantage of boundary layer ingesting propulsion systems (Refs. 6 to 8), which rely heavily on inlet distortion predictions. For numerical analyses, RANS methods are commonly used for many aerospace propulsion flows due to the reduced computational power relative to LES. Reynolds stress models (RSMs), which solve the individual transport equations for each of the Reynolds stresses, allow for a more detailed representation of the flow physics than the more commonly used one- and two-equation turbulence models. The objective of this paper is to investigate the use of RSMs to compute subsonic flow through an S-duct and transonic flow through a two-dimensional diffuser. Results are compared with computations made using the one-equation Spalart-Allmaras (SA) (Ref. 9) and two-equation Menter Shear-Stress Transport (SST) (Ref. 10) turbulence models.

2.0 Flow Solver

All simulations used the NASA's Fully Unstructured Navier-Stokes (FUN3D) code (Ref. 11). FUN3D is a node-based, production level code developed and maintained at the NASA Langley Research Center. It can solve the 2D/3D Euler and RANS equations for incompressible and compressible flows on unstructured grids. The FUN3D flow solver was chosen for two primary reasons: (1) its ability to simulate ducted diffusive flows on unstructured grids with various, well-validated turbulence models (Refs. 12 to 15) and (2) because it contains advanced models, such as RSMs (Ref. 15).

3.0 Inlet Distortion

The SAE ARP1420 Inlet Distortion parameters (Ref. 16) were used to compute the inlet distortion. These parameters included the circumferential average and tip distortions as computed by Equations (1) and (2) and the radial hub and tip distortions, as computed by Equations (4) and (5).

$$\mathrm{DPCP_{avg}} = \frac{1}{5}\sum_{i=1}^{5} \mathrm{DPCP}_i \tag{1}$$

$$\mathrm{DPCPT} = \frac{1}{2}\sum_{i=4}^{5} \mathrm{DPCP}_i \tag{2}$$

where

$$\mathrm{DPCP}_i = \mathrm{Intensity}_i \times \frac{\mathrm{Extent}_i}{150} \times \frac{1}{\mathrm{MPR}_i} \tag{3}$$

$$\mathrm{DPRPH}=\mathrm{DPRP}_1 \tag{4}$$

$$\mathrm{DPRPT}=\mathrm{DPRP}_5 \tag{5}$$

where

$$\mathrm{DPRP}_i = \frac{p_{\mathrm{avg,\,AIP}} - p_{\mathrm{avg},i}}{p_{\mathrm{avg,\,AIP}}} \tag{6}$$

4.0 Baseline IFCPT S-Duct

4.1 Geometry and Numerical Modeling

The modeled Inlet Flow Control and Prediction Technologies (IFCPT) S-duct geometry (Ref. 17), shown in Figure 1, consisted of an upstream bellmouth plenum, an S-duct, an aerodynamic interface plane (AIP) section, a constant area section extending five diameters downstream, and an adapter between the bellmouth plenum and the S-duct. The AIP total pressure instrumentation used in the experiment, shown in Figure 2, consisted of eight rakes distributed circumferentially in 45° increments, with each rake consisting of five total pressure probes. The probes were placed at the centers of equal areas as the SAE standard ARP1420 mandates (Ref. 16). Two versions of the AIP section were explored: one that modeled the AIP rakes and one that did not. The geometry without the rakes modeled in the AIP section is considered the baseline geometry and will be discussed in this section while the geometry that included the rakes will be discussed in Section 4.0.

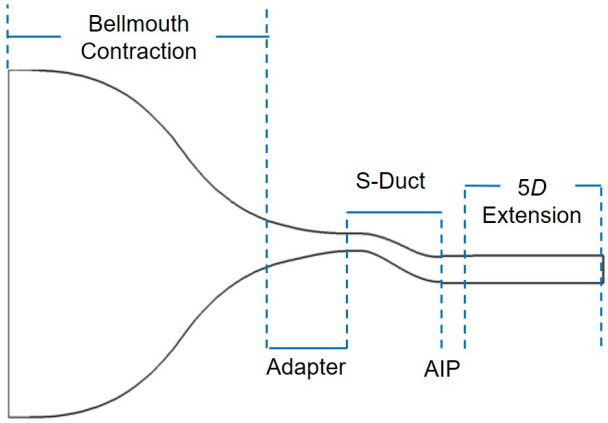

Figure 1.—Modeled IFCPT baseline S-duct geometry.

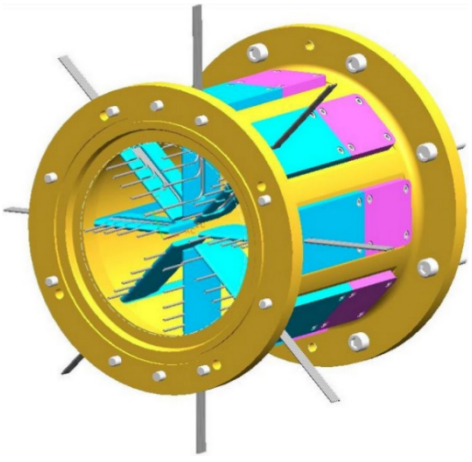

Figure 2.—AIP total pressure instrumentation (forward looking aft) (Ref. 17).

Initial grids were provided by the 4th AIAA Propulsion Aerodynamics Workshop (PAW) (Ref. 18) and consisted of two families of grids: multiblock structured and mixed-element unstructured. Initial wall spacing was set to 8.5×10^{-5} in. which translates to a $y^+ \sim 1.0$ at the condition specified in Table 1. Note that the mass flow rate given in Table 1 is area-averaged from the 40-probe AIP rake measurements. Node counts for these grids are listed in Table 2 and Table 3. Due to spanwise symmetry, only half of the geometry was modeled. The boundary conditions included subsonic inflow (which specified total pressure and total temperature), mass flow out, adiabatic viscous walls, and y-plane symmetry. Note that for the mass flow out boundary condition, the 40-probe rake measurement was used. Doing so is equivalent to using a mass flow rate derived from a 40 point grid and is not representative of a grid with significantly more points. This difference in effective grid resolution will introduce an error when comparing against the experiment as the simulation would have been run at a lower mass flow rate than the experiment.

Simulations on the workshop provided grids resulted in the prediction of a large separation bubble within the bellmouth plenum, with a significant amount of the flow going out the inflow plane, as depicted in Figure 3. To remedy this, the multiblock structured grids were modified to move the inflow plane further downstream. Once the inflow plane was moved, an upstream constant area section was added for numerical stability. All grid modifications were done using the Pointwise grid generation software (Ref. 19) and only the multiblock structured grids were modified in order to facilitate the initial truncation while keeping the majority of the grid intact. Geometry differences between the original and modified grids are shown in Figure 4 with the node counts listed in Table 4.

TABLE 1.—IFCPT S-DUCT
RUN CONDITION (REF. 18)

AIP Mach number	0.6294
Total pressure	14.3957 psi
Total temperature	529.11 °R
Mass flow rate[a]	5.5322 lbm/s

[a]Full-duct

TABLE 2.—NODE COUNTS FOR THE PAW PROVIDED
MULTIBLOCK STRUCTURED GRIDS

Grid level	Nodes ($\times 10^6$)
Coarse	6.92
Medium	10.92
Fine	19.97
Fine 1.5	42.23

TABLE 3.—NODE COUNTS FOR THE PAW PROVIDED
MIXED-ELEMENT UNSTRUCTURED GRIDS

Grid level	Nodes ($\times 10^6$)
Coarse	3.40
Medium	5.15
Fine	8.70
Fine 1.5	17.22

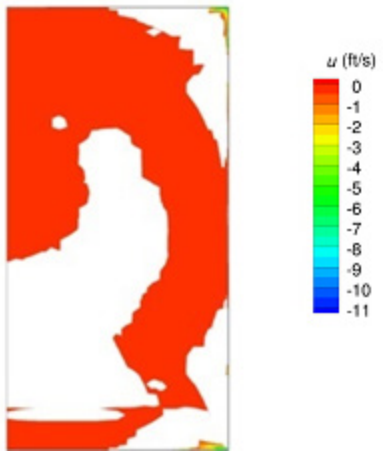

Figure 3.—Sample *u*-velocity contour plot at the inflow plane. Note that positive *u*-velocity is denoted by the white areas.

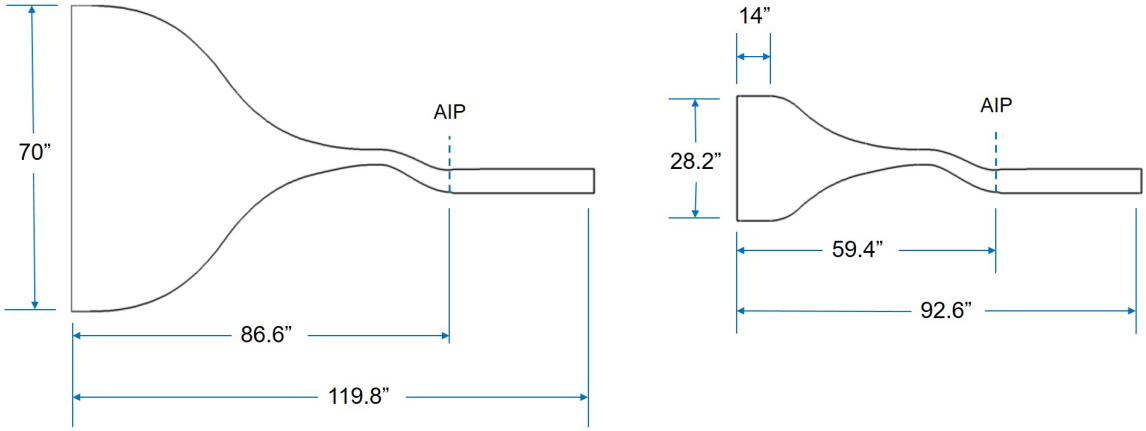

Figure 4.—Initial geometry (left) and modified geometry (right).

TABLE 4.—NODE COUNTS FOR THE MODIFIED MULTIBLOCK STRUCTURED GRIDS

Grid level	Nodes ($\times 10^6$)
Medium	10.48
Fine	19.24
Fine 1.5	40.08

4.2 Grid Convergence Study

A grid convergence study was completed on the modified grids using the SA turbulence model with and without the quadratic constitutive relation (QCR) (Ref. 20) for computing the turbulent stresses. The Roe flux construction scheme (Ref. 21) was used in conjunction with the van Leer flux limiter (Ref. 19) with a heuristic pressure limiter (Ref. 20). The flow was initialized with uniform flow at the run condition total pressure and total temperature with Mach numbers specified in Figure 5.

Figure 6 shows the wall static pressures on the various grids at the upper and lower surfaces while Figure 7 shows the wall static pressures on the various grids at the AIP. The results illustrate that the static pressures from the CFD simulations agree well with each other, but consistently under predict relative to the experiment. This is due to a known discrepancy between the mass flow rate used for the simulations and the actual experimental mass flow rate. Figure 8 and Figure 9 show the computed circumferential and radial distortion parameters as a function of the grid complexity *N*. As shown in Figure 8, the simulations that used the QCR predicted average and tip circumferential distortion values closer to the experiment compared to the simulations that did not use the QCR. From Figure 9 it can be seen that the use of the QCR did not have a significant impact in predicting the hub and tip radial distortion. Figure 10 shows the total pressure recovery as computed using the 40-point rake. From the figure it can be seen that use of the QCR did not have a significant impact in predicting the total pressure recovery. While not completely grid converged, it was decided to do the remaining baseline S-duct geometry simulations on the medium grid level grid. This would allow for a compromise between computational cost and accuracy.

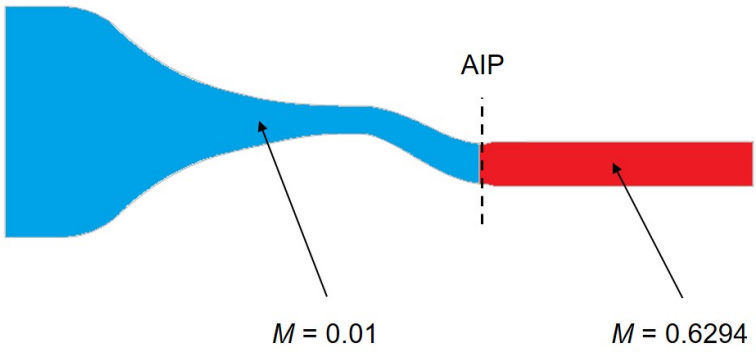

Figure 5.—Mach number flow initialization.

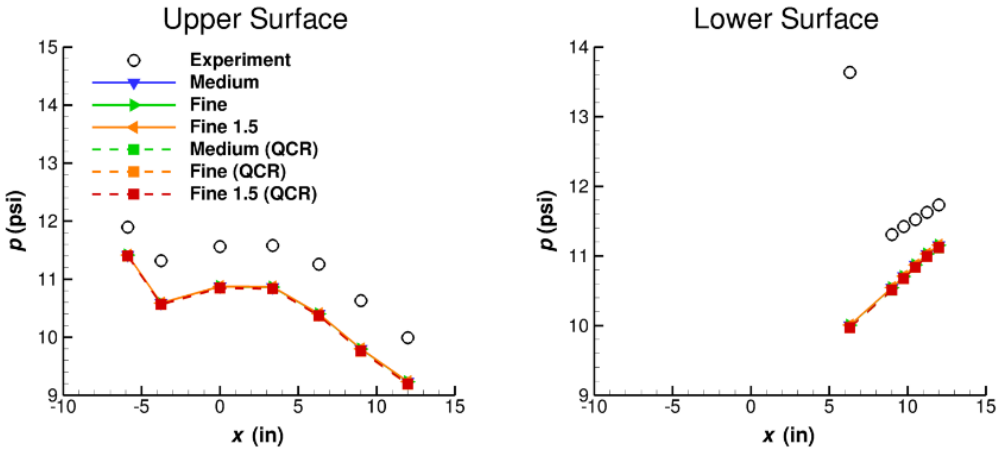

Figure 6.—Wall static pressures at the upper surface (left) and lower surface (right).

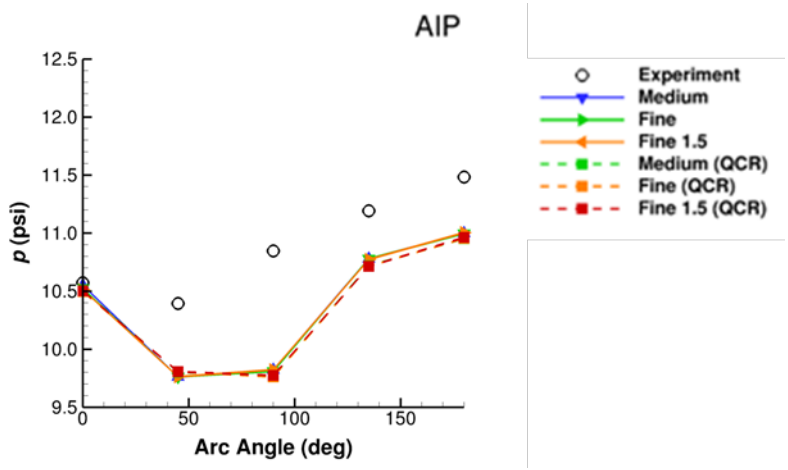

Figure 7.—Wall static pressures at the AIP.

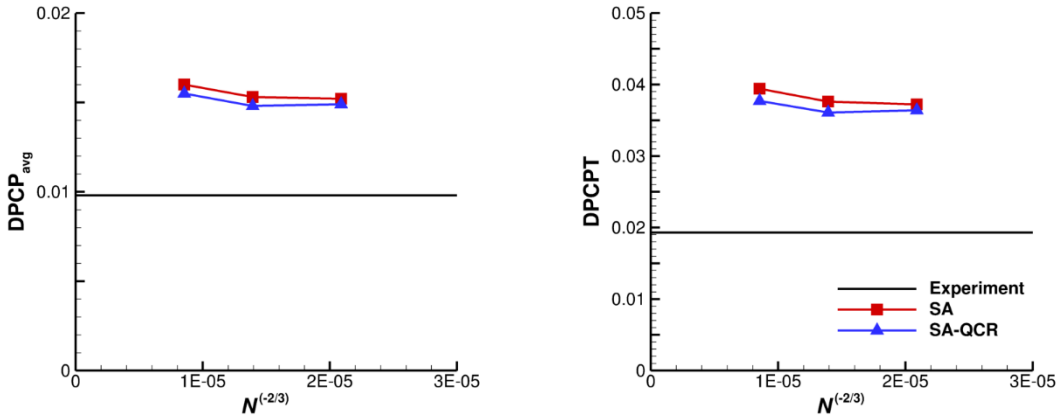

Figure 8.—Average (left) and tip (right) circumferential distortion as a function of grid complexity *N*.

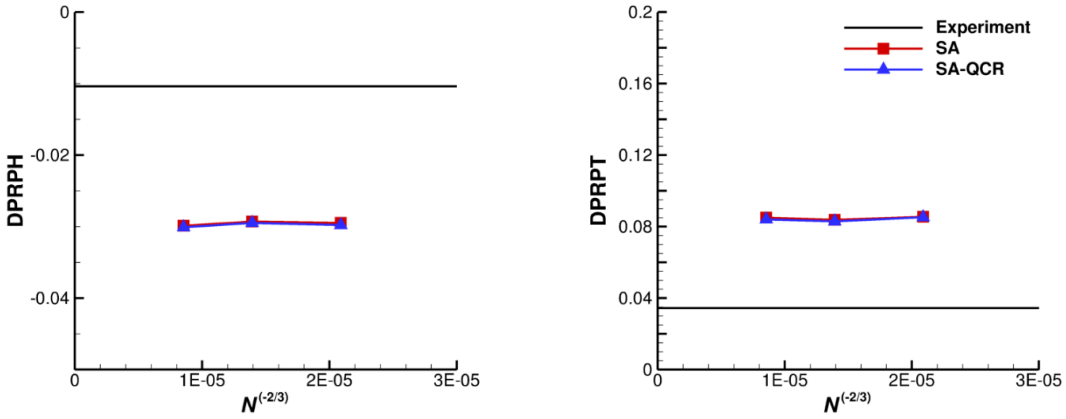

Figure 9.—Hub (left) and tip (right) radial distortion as a function of grid complexity *N*.

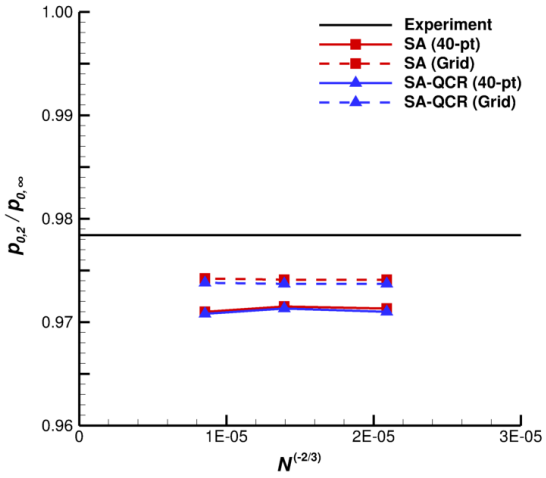

Figure 10.—Inlet total pressure recovery as a function of grid complexity *N*.

4.3 Turbulence Model Study

A turbulence model study was performed on the modified grid at the medium grid level. The additional turbulence models explored for the study included the Menter Shear-Stress Transport with the vorticity source term (SST-V) (Ref. 10) and the 2012 version of the Speziale-Sarkar-Gatski/Launder-Reece-Rodi (SSG/LRR) full RSM (Refs. 22 to 26). The SST-V turbulence model was run with and without the QCR while the SSG/LRR RSM was run with and without simple diffusion (SD) (Ref. 27). While the Roe flux construction scheme was still used, the flux limiter was changed to the van Albada flux limiter (Ref. 28) with a heuristic pressure limiter. The smooth limiter coefficient for the van Albada flux limiter was set to 1 and the limiter was frozen after 30,000 iterations. The change in the flux limiter was due to best practices of the baseline geometry simulated on structured grids, which are not presented in this paper. For each case, the flow was initialized with uniform flow at the run condition total pressure and total temperature at Mach 0.5.

Figure 11 and Figure 12 show eddy viscosity ratio contours at the AIP for the SA and SST-V turbulence model simulations with and without the QCR. The figures show that the simulations that used the SA turbulence model predicted higher eddy viscosity in the lower portion of the AIP compared to the simulations that used the SST-V turbulence model. It is also noted that the use of the QCR had little effect on the predicted eddy viscosity contours. Figure 13 to Figure 15 show the Reynolds *xy*-component shear stress contours at the AIP. These figures show that the regions of peak Reynolds *xy*-component shear stress magnitudes at the bottom portion of the AIP are largest for the SSG/LRR RSM simulations, followed by the SA turbulence model simulations, with the SST-V turbulence model simulations predicting the smallest regions. It is also noted that the use of the QCR, as well as simple diffusion, did not have a significant effect on the predicted Reynolds *xy*-component shear stress contours.

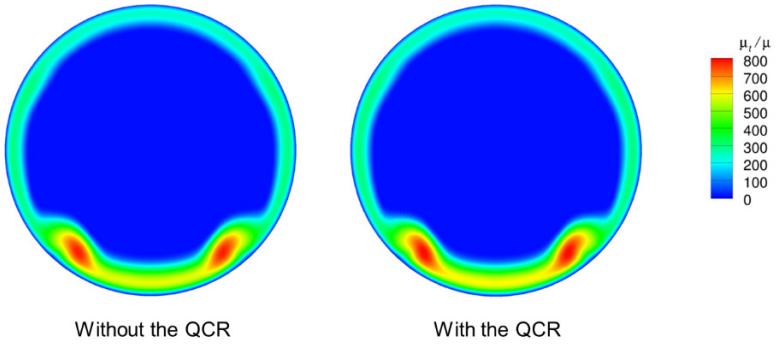

Figure 11.—Eddy viscosity ratio contours at the AIP for the SA turbulence model simulations without (left) and with (right) the QCR.

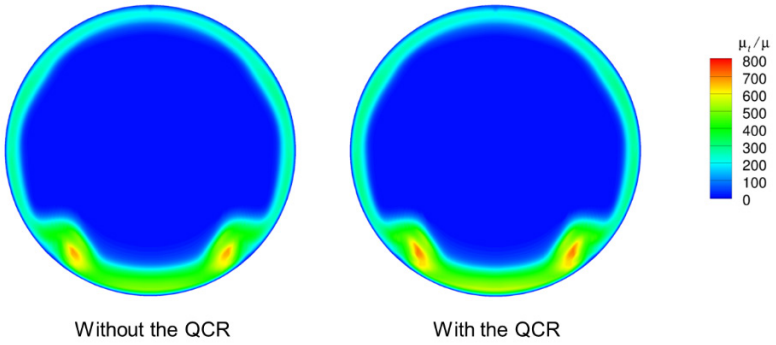

Figure 12.—Eddy viscosity ratio contours at the AIP for the SST-V turbulence model simulations without (left) and with (right) the QCR.

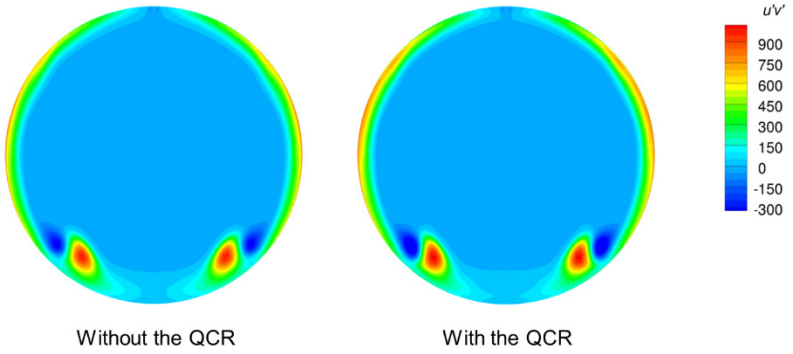

Figure 13.—Reynolds *xy*-component shear stress contours at the AIP for the SA turbulence model simulations without (left) and with (right) the QCR.

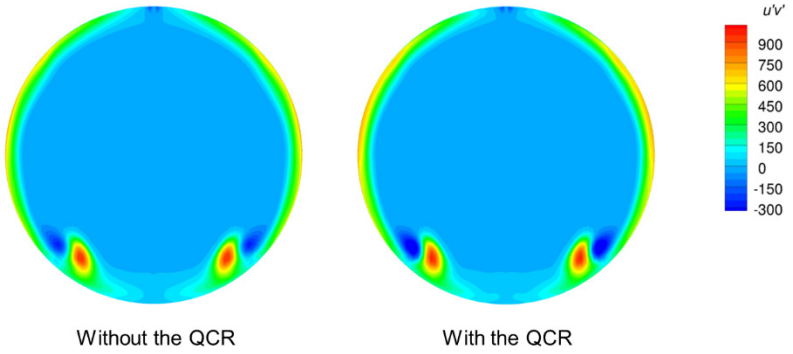

Figure 14.—Reynolds *xy*-component shear stress contours at the AIP for the SST-V turbulence model simulations without (left) and with (right) the QCR.

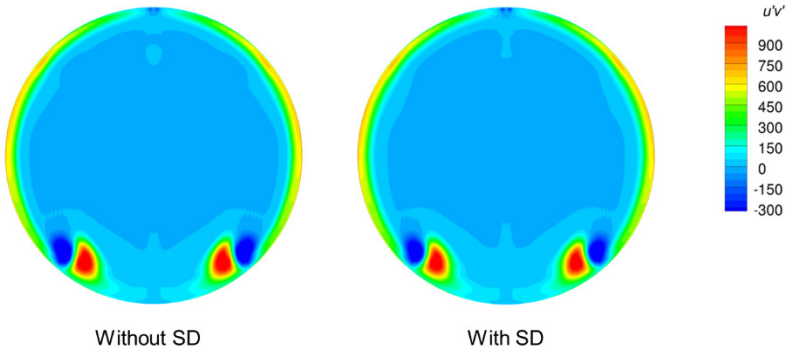

Figure 15.—Reynolds *xy*-component shear stress contours at the AIP for the SSG/LRR RSM simulations without (left) and with (right) simple diffusion.

Figure 16 shows the computed inlet distortion parameters. From the figure it can be noted that the simulations that used the SSG/LRR RSM better predicted the circumferential and radial inlet distortion compared to the simulations that used the SA and SST-V turbulence models. Figure 17 shows the computed 40-point total pressure recovery as a function of mass flow rate at the AIP, which shows that while all the simulations underpredicted the total pressure recovery, the simulations that used the SSG/LRR RSM best matched the experimental value. The reason that the simulations using the RSM outperformed the simulations using the SA and SST-V turbulence models for predicting inlet performance is due to the differences in the predicted Reynolds stresses.

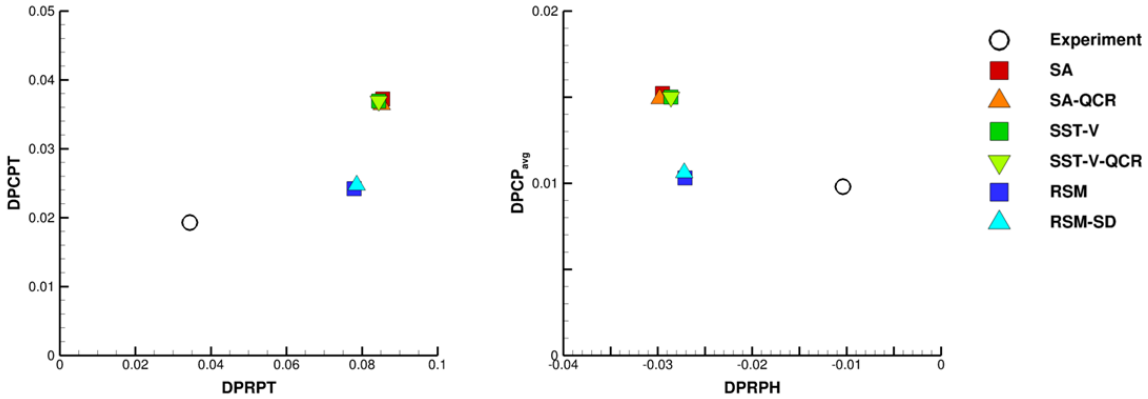

Figure 16.—Tip distortion (left) and circumferential average vs. radial hub (right) distortion for the modified baseline geometry simulations.

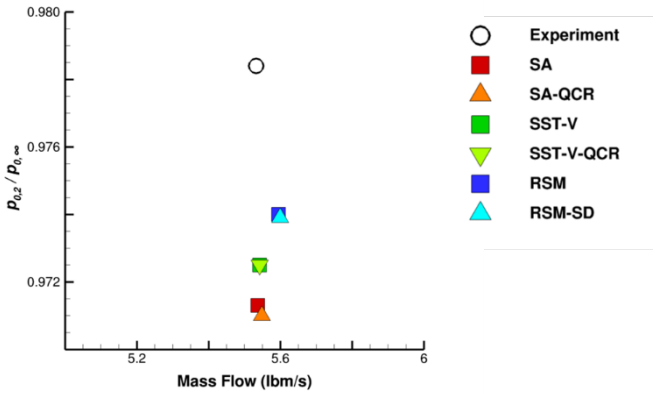

Figure 17.—Inlet total pressure recovery vs. mass flow rate at the AIP for the modified baseline geometry simulations.

5.0 IFCPT S-Duct with AIP Rakes

5.1 Geometry and Numerical Modeling

The modeled IFCPT S-duct with AIP rakes geometry, shown in Figure 18, is the same as the baseline geometry with the exception that the AIP rakes are now modeled. The grids used to simulate this geometry were a set of mixed-element unstructured grids developed by Carter et al. (Ref. 14), with viscous spacing set such that the y^+ would be ~1.0 and consistent with the PAW provided meshes. The simulations were run at the condition outlined in Table 1. Node counts for the grids are listed in Table 5. Due to spanwise symmetry, only half of the geometry was modeled.

The run condition for the IFCPT S-duct with AIP rakes was the same as the baseline S-duct configuration and used the same boundary conditions. Simulations were performed using the SA with the QCR, SST-V, and SST turbulence models, as well as the 2012 version of the SSG/LRR RSM. The Roe flux construction scheme was used in conjunction with the van Albada flux limiter with a heuristic pressure limiter. The smooth limiter coefficient for the van Albada flux limiter was set to 1 and the limiter was frozen after 30,000 iterations. The flow was initialized with uniform flow at the run condition total pressure and total temperature at Mach 0.5.

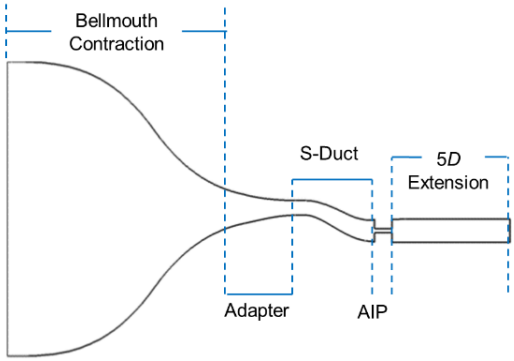

Figure 18.—Modeled IFCPT S-duct with AIP rakes geometry.

TABLE 5.—NODE COUNTS FOR THE MIXED-ELEMENT UNSTRUCTURED GRIDS

Grid level	Nodes ($\times 10^6$)
Medium	6.71
Fine	9.27

5.2 Results

Figure 19 to Figure 21 show the eddy viscosity contours at the AIP for the various turbulence model simulations. The figures show that the simulations that modeled the AIP rakes predicted lower eddy viscosity values at the bottom portion of the AIP compared to the simulations of the baseline configuration. Figure 22 to Figure 25 show the Reynolds *xy*-component shear stress contours at the AIP for the various turbulence model simulations. The figures show that the simulations that modeled the AIP rakes predicted higher Reynolds *xy*-component shear stress magnitudes at the bottom portion of the AIP compared to the simulations of the baseline configuration. Overall, the solutions on the medium and fine grids for the cases with the AIP rakes modeled agreed well with each other. The exception to this is the simulation on the fine grid using the SST turbulence model. It is suspected that turbulence is being generated at the inflow plane and is not dissipating downstream for that particular case. This is shown in Figure 26, which are eddy viscosity contour plots on the center plane for the medium and fine grid level solutions. It is also shown at various axial stations between the inflow plane and AIP as defined in Table 6 and shown in Figure 27 and Figure 28.

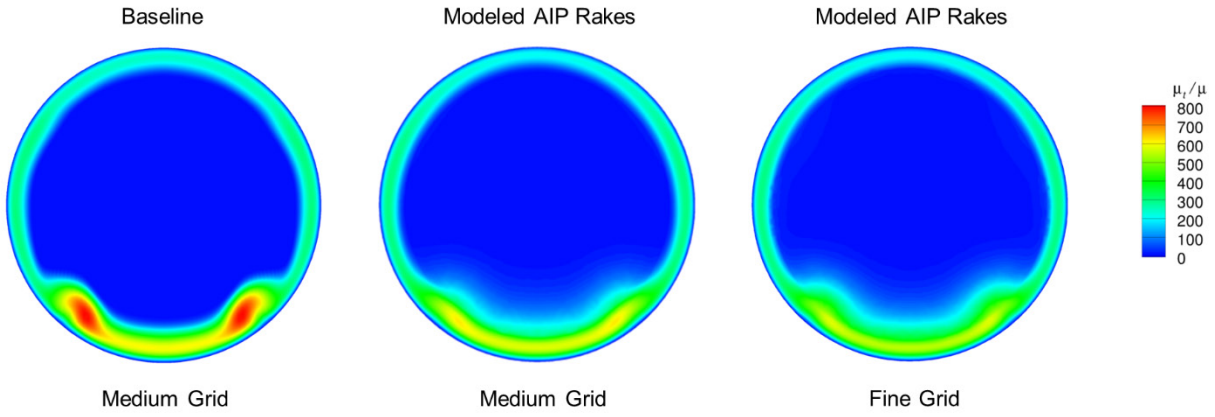

Figure 19.—Eddy viscosity contours at the AIP for the baseline geometry on the medium grid (left), modeled AIP rake geometry on the medium grid (middle), and modeled AIP rake geometry on the fine grid (right) using the SA-QCR turbulence model.

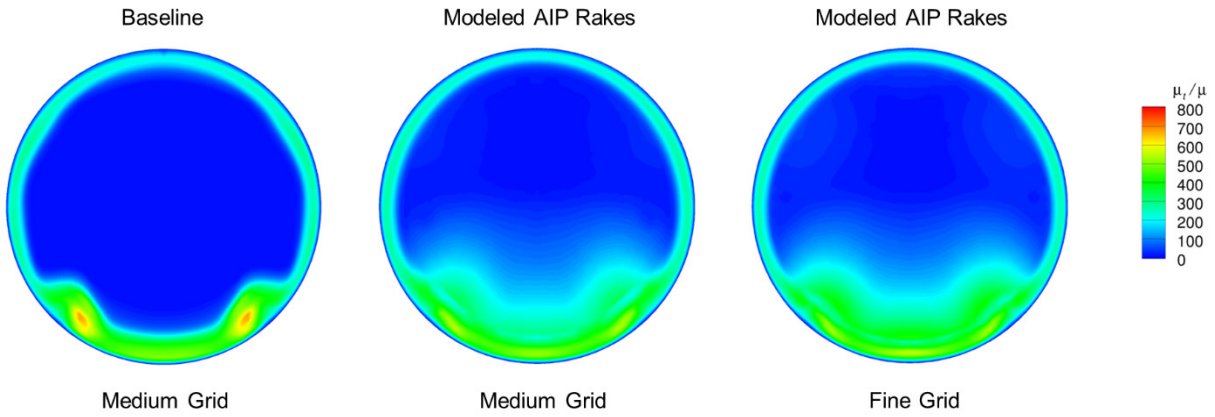

Figure 20.—Eddy viscosity contours at the AIP for the baseline geometry on the medium grid (left), modeled AIP rake geometry on the medium grid (middle), and modeled AIP rake geometry on the fine grid (right) using the SST-V turbulence model.

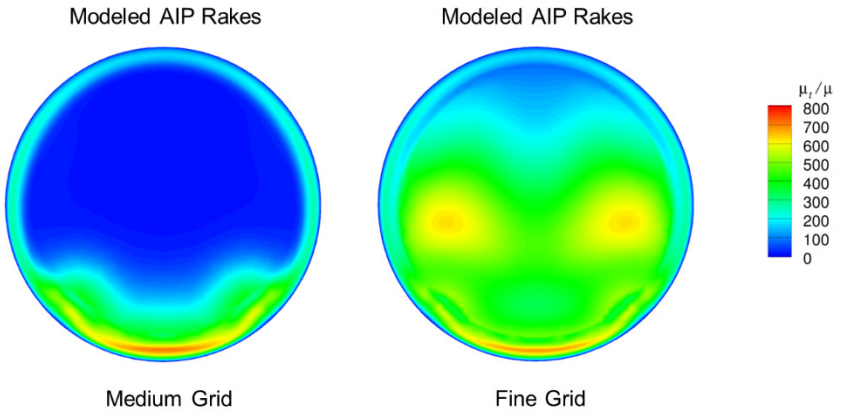

Figure 21.—Eddy viscosity contours at the AIP for the modeled AIP rake geometry on the medium grid (left) and on the fine grid (right) using the SST turbulence model.

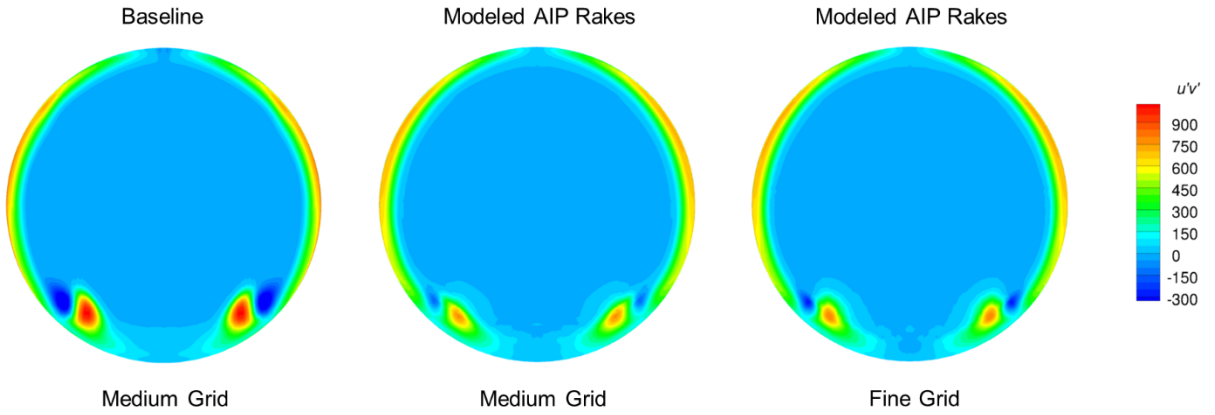

Figure 22.—Reynolds *xy*-component shear stress contours at the AIP for the baseline geometry on the medium grid (left), modeled AIP rake geometry on the medium grid (middle), and modeled AIP rake geometry on the fine grid (right) using the SA-QCR turbulence model.

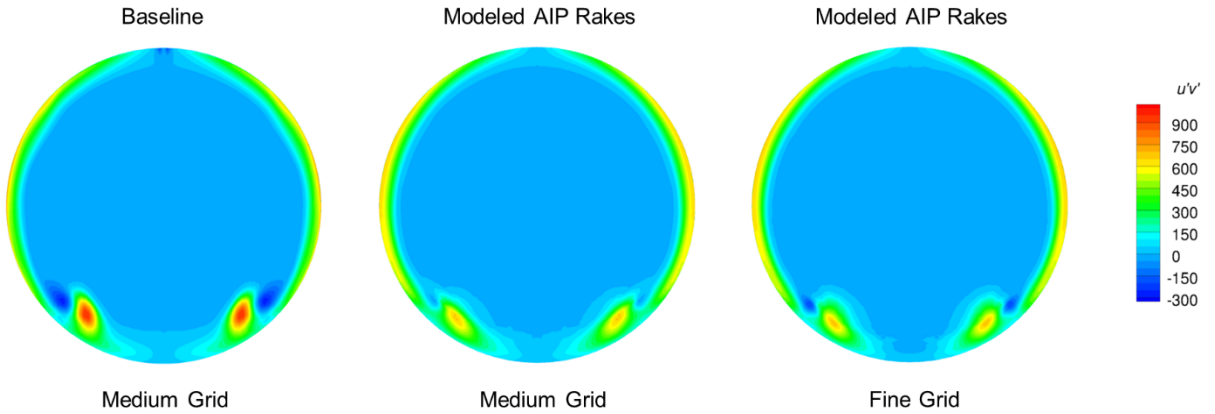

Figure 23.—Reynolds *xy*-component shear stress contours at the AIP for the baseline geometry on the medium grid (left), modeled AIP rake geometry on the medium grid (middle), and modeled AIP rake geometry on the fine grid (right) using the SST-V turbulence model.

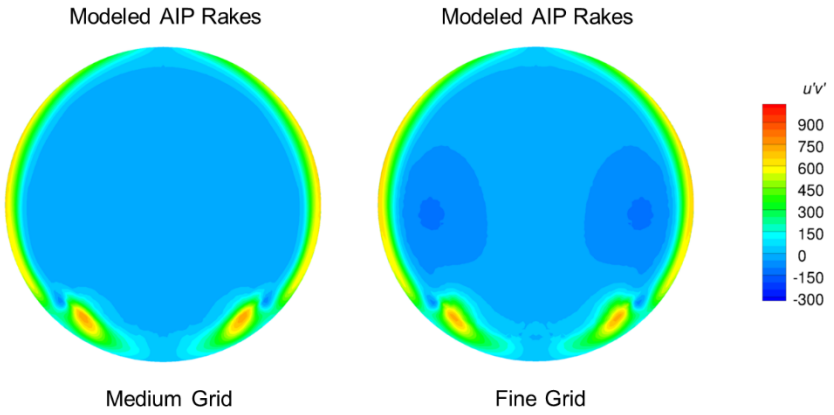

Figure 24.—Reynolds *xy*-component shear stress contours at the AIP for modeled AIP rake geometry on the medium grid (left) and on the fine grid (right) using the SST turbulence model.

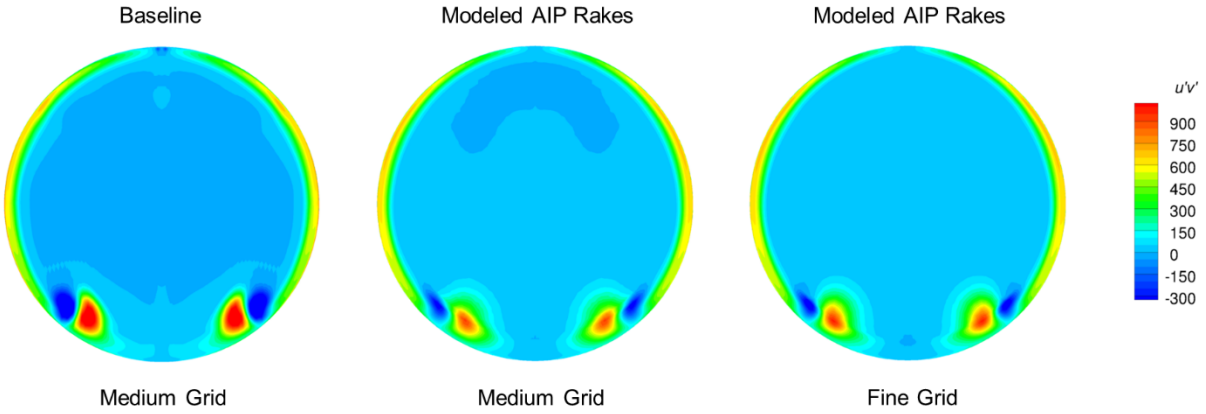

Figure 25.—Reynolds *xy*-component shear stress contours at the AIP for the baseline geometry on the medium grid (left), modeled AIP rake geometry on the medium grid (middle), and modeled AIP rake geometry on the fine grid (right) using the SSG/LRR RSM.

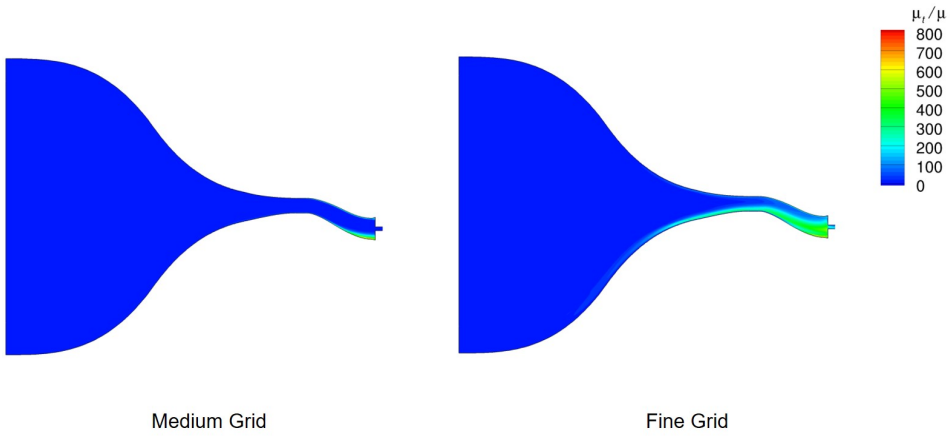

Figure 26.—Center plane eddy viscosity contours for the modeled AIP rake geometry using the SST turbulence model on the medium grid (left) and fine grid (right).

TABLE 6.—AXIAL STATION LOCATIONS

Station no.	Percent[a]
1	10
2	50
3	90

[a] $\text{Percent} = \dfrac{x_{\text{station}} - x_{\text{AIP}}}{x_{\text{inflow}} - x_{\text{AIP}}}$

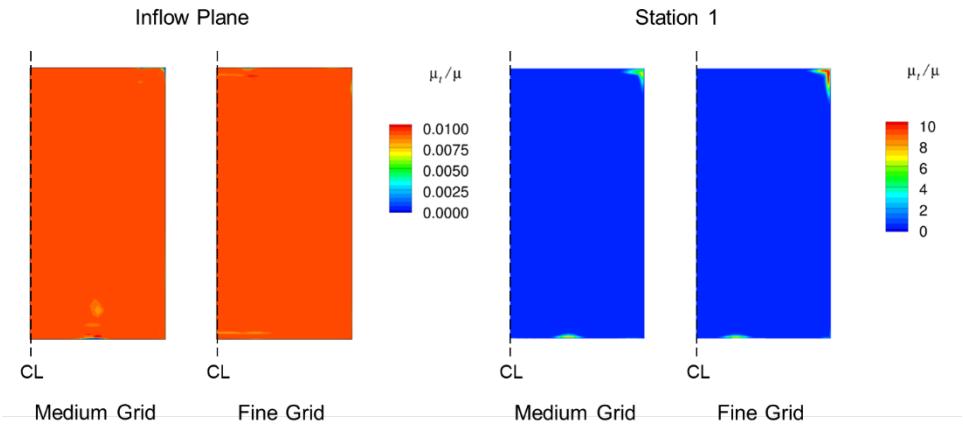

Figure 27.—Eddy viscosity contours at the inflow plane (left) and Station 1 (right) for the modeled AIP rake geometry using the SST turbulence model.

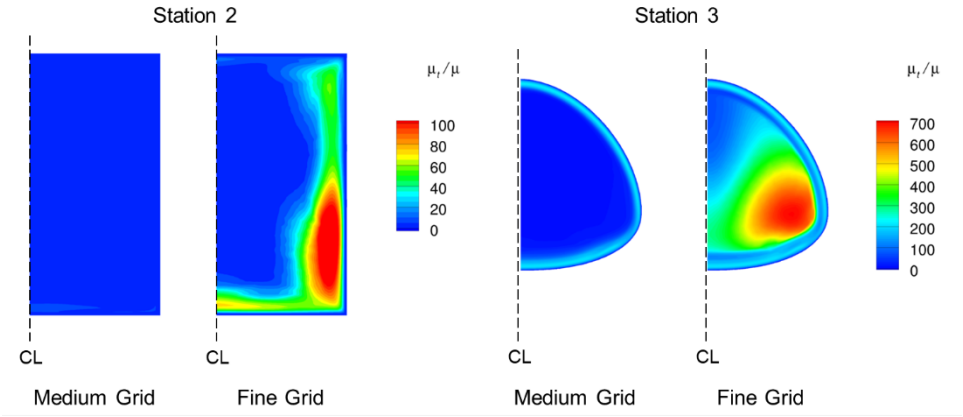

Figure 28.—Eddy viscosity contours at Station 2 (left) and Station 3 (right) for the modeled AIP rake geometry using the SST turbulence model.

5.3 Additional Simulations

Four additional steady-RANS simulations were performed of the modeled AIP rake geometry with the SST turbulence model on the fine grid. This was done in order to better understand why the default simulation predicted higher than expected eddy viscosity and Reynolds *xy*-component shear stress magnitudes at the AIP. Each simulation modified a different FUN3D input parameter, as outlined in Table 7. The first simulation changed the flux construction scheme to the low dissipation version of the Roe flux construction scheme (Ref. 29). The second simulation ran first-order spatial iterations until convergence was achieved before switching to second-order spatial iterations. The third simulation reduced the maximum mean-flow and turbulence equations CFL numbers from 100 and 10 to 25 and 5, respectively, while the fourth simulation initialized the flow field at Mach 0.01 instead of Mach 0.5.

Figure 29 to Figure 32 show eddy viscosity contour plots at the AIP for the additional simulations as compared to the simulation on the medium grid and on the fine grid with the default settings. The figures show that changing the flux construction scheme had little impact on the predicted flow field, while reducing either the flow initialization Mach number or the maximum mean-flow and turbulence CFL numbers predicted flow fields resembling the one predicted on the medium grid with the default settings. This is further evidenced in the inlet distortion and total pressure recovery, shown in Figure 33 and Figure 34, respectively.

TABLE 7.—MODIFIED PARAMETERS OF THE ADDITIONAL MODELED AIP RAKE GEOMETRY SIMULATIONS

Simulation no.	Parameter	Old value	New value
1	Flux construction	Roe	low dissipation Roe
2	First-order iterations	0	38,000
3	Max mean-flow CFL number	100	25
	Max turbulence CFL number	10	5
4	Flow initialization Mach number	0.5	0.01

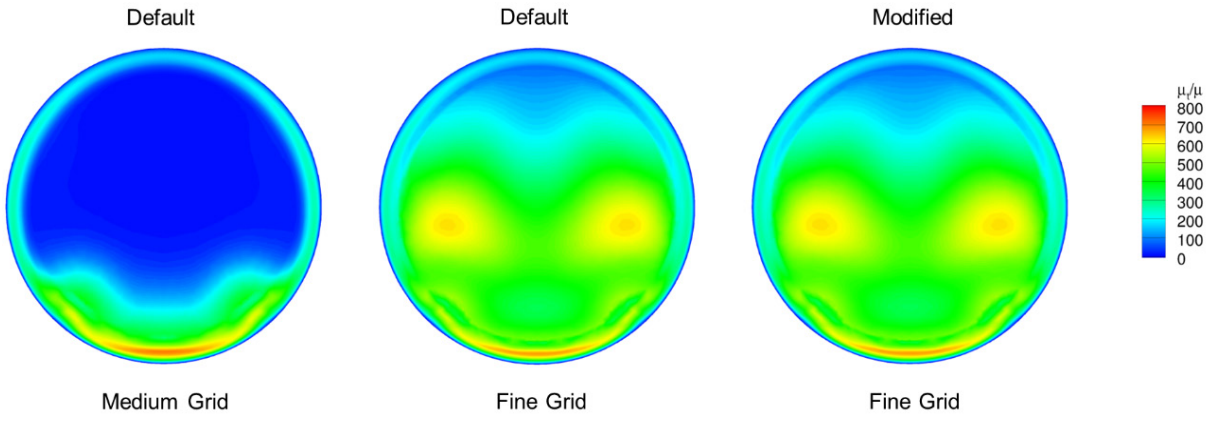

Figure 29.—Eddy viscosity contours at the AIP with the default settings on the medium grid (left), the default settings on the fine grid (middle), and the modified settings that used the alternate flux construction scheme on the fine grid (right).

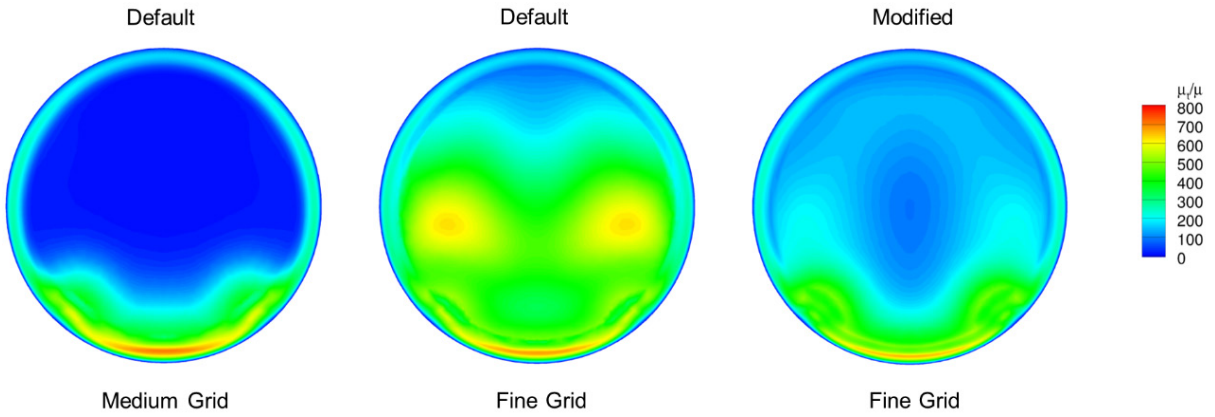

Figure 30.—Eddy viscosity contours at the AIP with the default settings on the medium grid (left), the default settings on the fine grid (middle), and the modified settings that used first-order iterations on the fine grid (right).

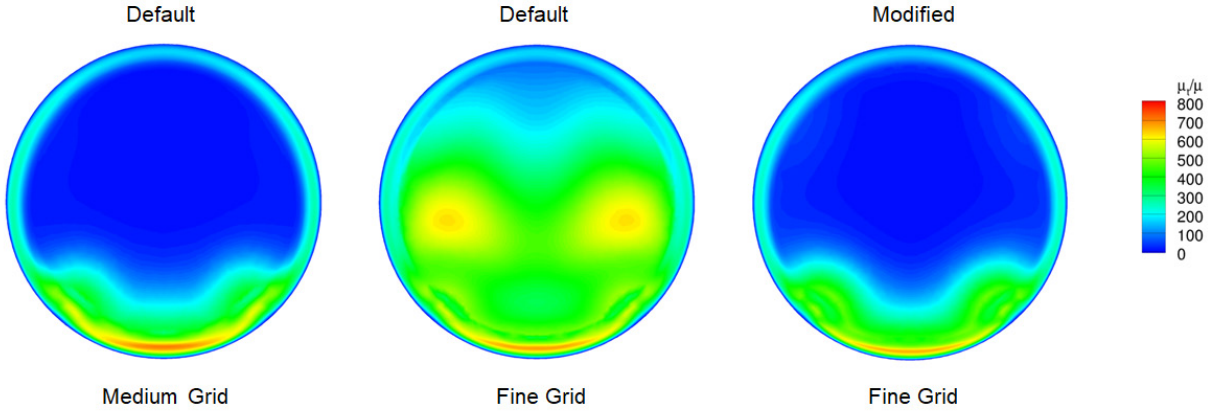

Figure 31.—Eddy viscosity contours at the AIP with the default settings on the medium grid (left), the default settings on the fine grid (middle), and the modified settings that used lower maximum CFL numbers on the fine grid (right).

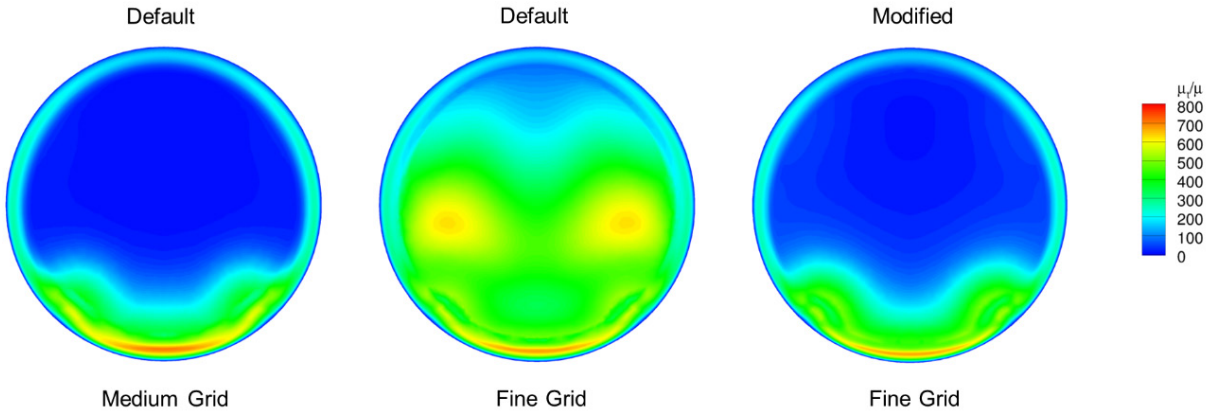

Figure 32.—Eddy viscosity contours at the AIP with the default settings on the medium grid (left), the default settings on the fine grid (middle), and the modified settings that used the lower flow initialization Mach number on the fine grid (right).

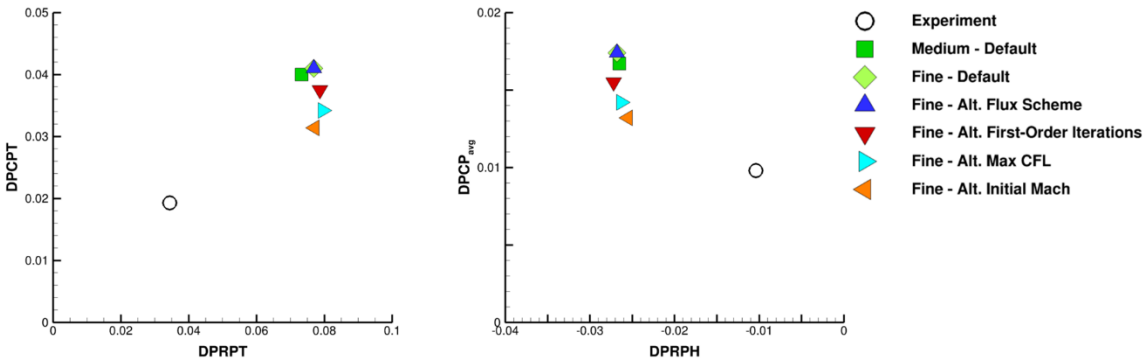

Figure 33.—Tip distortion (left) and circumferential average vs. radial hub (right) distortion for the SST turbulence model simulations of the modeled AIP rake geometry.

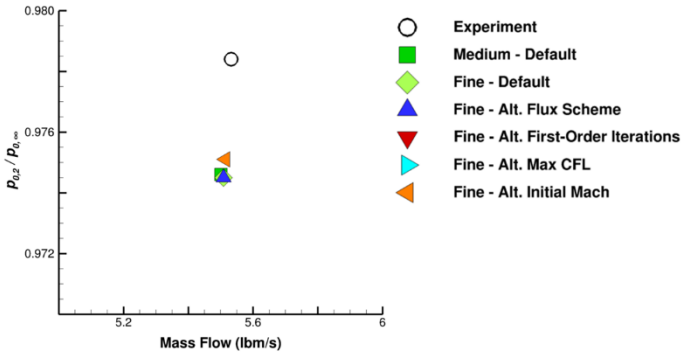

Figure 34.—Inlet total pressure recovery vs. mass flow rate at the AIP for the SST turbulence model simulations of the modeled AIP rake geometry.

6.0 Sajben Diffuser

6.1 Geometry and Numerical Modeling

The Sajben diffuser (Ref. 30), shown in Figure 35, is a two-dimensional transonic diffuser with a strong shock-induced separation. The dimensions in Figure 35 are shown with respect to the throat height of 1.7322. For simulation purposes, a constant area section was added that extended ten throat heights downstream of the diffuser exit station. A mixed-element unstructured grid was used to simulate the diffuser. The grid consisted of 54.9×10^5 nodes and featured hexahedral elements near the wall and tetrahedral elements in the core. Viscous spacing was set such that the y^+ would be ~1.0 at the run condition outlined in Table 8. The boundary conditions included adiabatic viscous walls, subsonic inflow, and subsonic outflow (which specified a back pressure). It was found that setting the back pressure to 14.775 psi allowed the normal shock to form at the desired location within the throat.

A turbulence model study was performed that looked at the SA and SST-V turbulence models (each with and without the QCR), as well as the 2012 and 2019 (Ref. 31) versions of the SSG/LRR RSM. Note that the 2012 version of the SSG/LRR RSM was run with and without simple diffusion. All simulations used the Roe flux construction scheme.

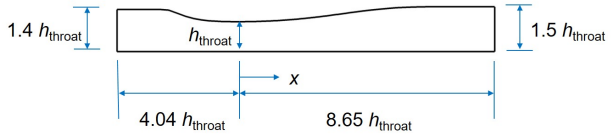

Figure 35.—Sajben diffuser geometry, h_{throat} = 1.7322 in.

TABLE 8.—SAJBEN DIFFUSER RUN CONDITION

Inflow Mach number	0.9
Total pressure	19.58 psi
Total temperature	540 °R

6.2 Results

Figure 36 shows the static pressure profiles on the bottom and top walls, with the axial stations nondimensionized by the throat height of 1.7322 in. It can be seen that all the simulations predict the same static pressure profiles up until the normal shock, at which point the simulations predict varying profiles. The simulations that used the RSM better predicted the normal shock location but overpredicted the downstream static pressure compared to the simulations that used the SA and SST-V turbulence models. This was regardless of which version of the RSM was used (i.e., 2012, 2019, 2012 with simple diffusion). It is also noted that the simulations that used the QCR fared slightly worse at predicting the normal shock location and downstream static pressure compared to the simulations that did not use the QCR.

Figure 37 and Figure 38 shows select u-velocity profiles. It can be seen that the boundary layer thickness significantly increases through the shock wave and in the subsequent divergent section of the diffuser. This shows that the viscous interaction effects can be substantial and result in complicated interactions between the shock wave and the separated boundary layer. It is also shown that the simulations that used the SA turbulence model predicted flow separation from x/h_{local} = 2.9 through x/h_{local} = 7.5 while the simulations that used the SST-V turbulence model predicted flow reattachment by x/h_{local} = 7.5. This is in contrast to the simulations that used the RSM, which predicted flow reattachment by x/h_{local} = 6.4. Note that the axial locations have been non-dimensionalized by the local duct height. Another observation was that the simulations that used the SA and SST-V turbulence models better predicted the onset separation strength while the simulations that used the RSM better predicted the flow reattachment and the adverse pressure gradient boundary layer profiles. This is further evidenced in the u_{rms} profiles, shown in Figure 39 and Figure 40. It is also noted from Figure 39 and Figure 40 that the addition of the QCR led to better prediction of the u_{rms} profiles while the simulations that used the RSM overall better predicted the u_{rms} profiles.

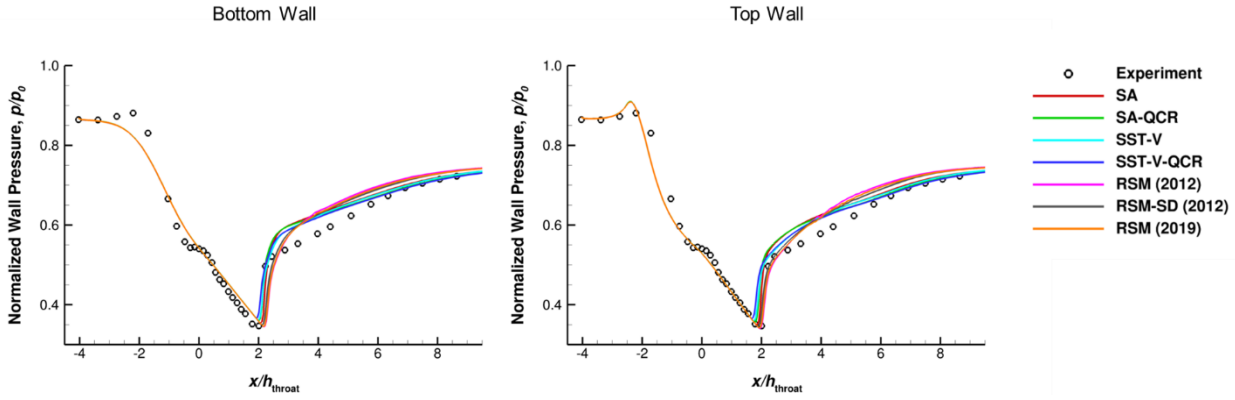

Figure 36.—Static pressure profiles on the bottom (left) and top (right) walls, h_{throat} = 1.7322 in.

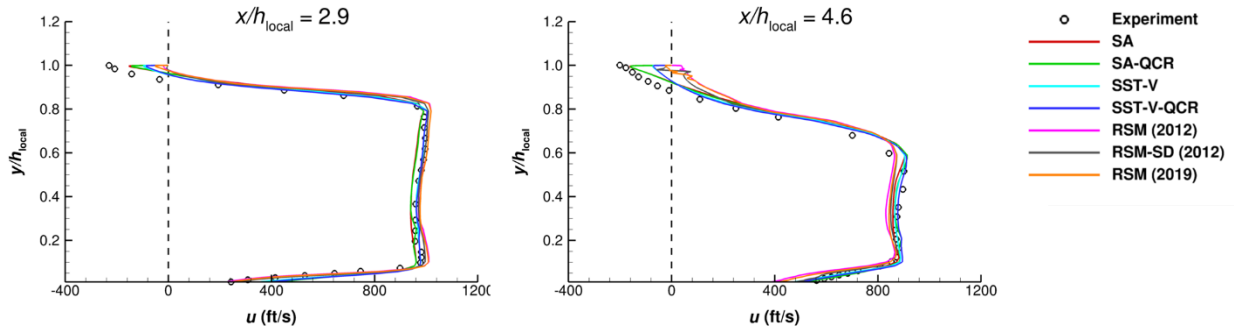

Figure 37.—*U*-velocity profiles at x/h_{local} = 2.9 (left) and at x/h_{local} = 4.6 (right).

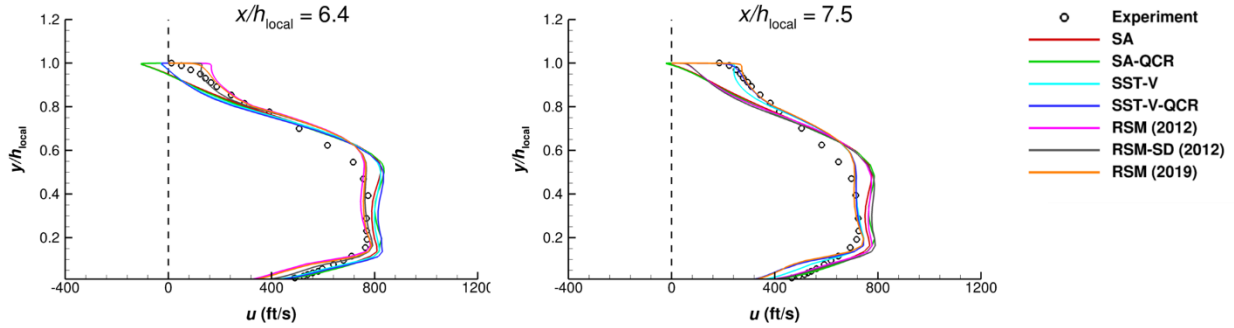

Figure 38.—*U*-velocity profiles at x/h_{local} = 6.4 (left) and at x/h_{local} = 7.5 (right).

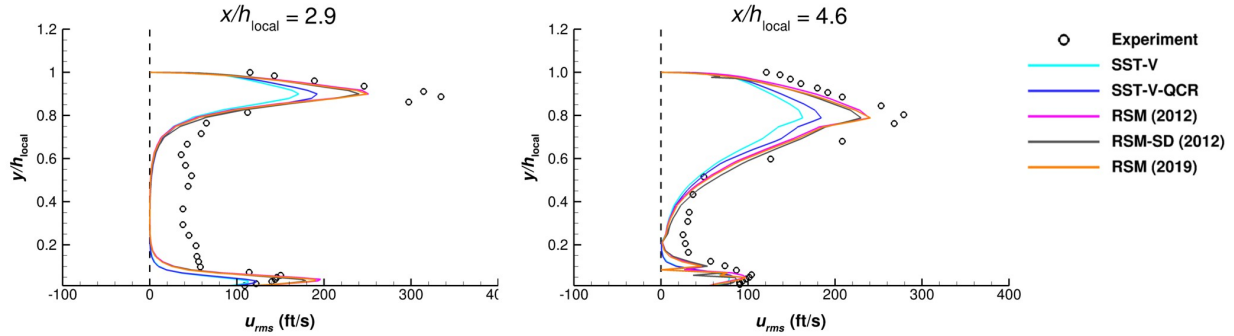

Figure 39.—U_{rms} profiles at x/h_{local} = 2.9 (left) and at x/h_{local} = 4.6 (right).

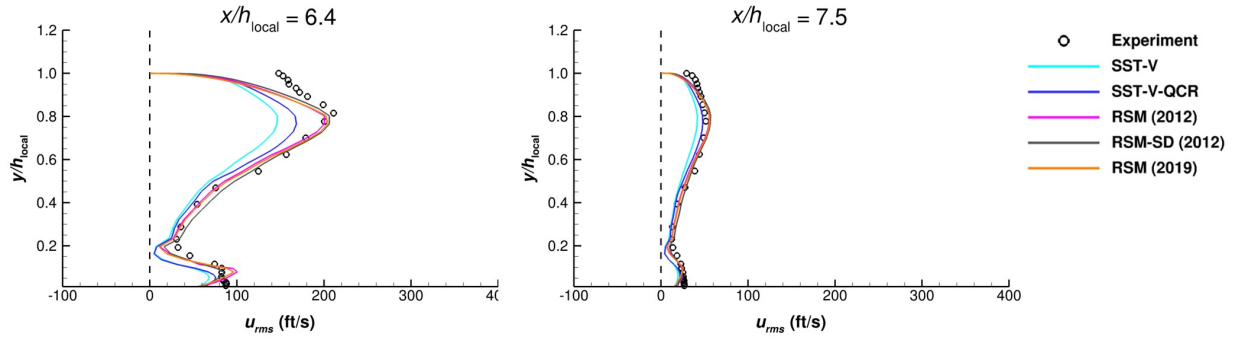

Figure 40.—U_{rms} profiles at x/h_{local} = 6.4 (left) and at x/h_{local} = 7.5 (right).

7.0 Conclusions

FUN3D steady-RANS simulations were performed for subsonic flow in an S-duct diffuser and transonic flow in a two-dimensional diffuser. The simulations explored the use of the SA and SST turbulence models as well as the SSG/LRR RSM for predicting the turbulent flow. The S-duct simulation results showed that the use of the SSG/LRR RSM enabled improvements over the standard turbulence models in predicting inlet distortion and total pressure recovery while the transonic diffuser simulation results showed that the SSG/LRR RSM enabled improvements over the standard turbulence models in predicting the boundary layer reattachment, adverse pressure gradient, and rms-velocity profiles. The RSMs provided improved results compared to the more traditionally used turbulence models, SA and SST, for the simulation of these diffusing flows.

References

1. Gregg, R., "The Challenges of Certification by Analysis," Presented at the 13th Symposium on Overset Composite Grids and Solution Technology, Mukilteo, WA, 2016.
2. Slotnick, J.P., and Mavriplis, D.J., "A Grand Challenge for the Advancement of Numerical Prediction of High Lift Aerodynamics," AIAA-2021-0955, January 2021.
3. Olivares, G., "Certification Analysis I and II," Presented at the FAA JAMS 2010 Technical Review Meeting, Seattle, WA, 2010.
4. Slotnick, J.P., Khodadoust, A., Alonso, J., Darmofal, D., Gropp, W., Lurie, E., and Mavriplis, D., "CFD Vision 2030 Study: A Path to Revolutionary Computational Aerosciences," NASA/CR-2014-218178, March 2014.
5. "NASA Aeronautics Strategic Implementation Plan 2019 Update," NASA Aeronautics Strategic Implementation Plan, URL: https://www.nasa.gov/sites/default/files/atoms/files/sip-2019-v7-web.pdf [cited 30 March 2021].
6. Bradley, M.K., and Droney, C.K., "Subsonic Ultra Green Aircraft Research Phase II: N+4 Advanced Concept Development," NASA/CR—2012-217556, May 2012.
7. Kim, H.D., Brown, G.V., and Felder, J.L., "Turboelectric Distributed Propulsion in a Hybrid Wing Body Aircraft," *20th International Society for Air Breathing Engines*, ISABE-2011-1340, Gothenburg; Sweden, 2011.
8. Bowman, C.L., Felder, J.L., and Marien, T.V., "Turbo- and Hybrid-Electrified Aircraft Propulsion for Commercial Transport," AIAA-2018-4984, July 2018.
9. Spalart, P., and Allmaras, S., "A One-Equation Turbulence Model for Aerodynamic Flows," *La Recherche Aerospatiale*, no. 1, 1984, pp. 5–21.
10. Menter, F.R., "Improved Two-Equation k-omega Turbulence Models for Aerodynamic Flows," NASA/TM-103975, October 1992.
11. Biedron, R.T., Carlson, J.-R., Derlaga, J.M., Gnoffo, P.A., Hammond, D.P., Jones, W.T., Kleb, B., Lee-Rausch, E.M., Nielson, E.J., Park, M.A., Rumsey, C.L., Thomas, J.L., Thompson, K.B., and Wood, W.A., "FUN3D Manual: 13.6," NASA/TM—2019-220416, October 2019.
12. Davis, Z.S., and Park, M.A., "IFCPT S-Duct Grid-Adapted FUN3D Computations for the Third Propulsion Aerodynamics Workshop," AIAA-2017-4835, July 2017.
13. Winkler, C.M., and Davis, Z.S., "Summery of the 3rd Propulsion Aerodynamics Workshop: S-Duct Results," AIAA-2017-4912, July 2017.
14. Carter, M., Bozeman, M., and Carlson, J.-R., "FUN3D and USM3D Analysis of the Propulsion Aerodynamics Workshop 2018 S-duct Test Case," AIAA-2019-3848, August 2019.

15. Dudek, J.C., and Carlson, J.-R., "Evaluation of Full Reynolds Stress Turbulence Models in FUN3D," AIAA-2017-0541, January 2017.
16. Society of Automotive Engineers Inc., "Gas Turbine Engine Inlet Flow Distortion Guidelines," ARP 1420 Rev. B, 2011.
17. McMillan, M.L., Gissen, A., Vukasinovic, B., Lakebrink, M.T., Glezer, A., Mani, M., and Mace, J., "Inlet Flow Control and Prediction Technologies for Embedded Propulsion Systems: Summary Report for Fiscal Year 2009," NASA/CR—2010-216779, October 2010.
18. Babcock, D.A., Neto, L.T., and Davis, Z.S., "Summery of the 4th Propulsion Aerodynamics Workshop: S-Duct Results," AIAA-2019-3845, August 2019.
19. Pointwise, Software Package, Version 18.3 Release 1, Pointwise Inc., Fort Worth, TX, 2019.
20. Spalart, P.R., "Strategies for Turbulence Modelling and Simulations," *International Journal of Heat and Fluid Flow*, vol. 21, no. 33, 2000, pp. 252–263.
21. Roe, P.L., "Approximate Riemann Solvers, Parameter Vectors, and Difference Schemes," *Journal of Computational Physics*, vol. 43, no. 2, 1981, pp. 357–372.
22. Van Leer, B., "Towards the Ultimate Conservative Difference Scheme II. Monotonicity and Conservation Combined in a Second Order Scheme," *Journal of Computational Physics*, vol. 14, no. 4, 1974, pp. 361–370.
23. Park, M.A., and Darmofal, D.L., "Output-Adaptive Tetrahedral Cut-Cell Validation for Sonic Boom Prediction," AIAA-2008-6594, August 2008.
24. Eisfeld, B., Rumsey, C., and Togiti, V., "Verification and Validation of a Second-Moment-Closure Model," *AIAA Journal*, vol. 54, no. 5, 2016, pp. 1524–1541.
25. Eisfeld, B., Rumsey, C., and Togiti, V., "Erratum: Verification and Validation of a Second-Moment-Closure Model," *AIAA Journal*, vol. 54, no. 9, 2016, p. 2926.
26. Cecora, R.-D., Radespiel, R., Eisfeld, B., and Probst, A., "Differential Reynolds-Stress Modeling for Aeronautics," *AIAA Journal*, vol. 53, no. 3, 2015, pp. 739–755.
27. Eisfeld, B., "Implementation of Reynolds Stress Models into the DLR-FLOWer Code," Institutsbericht, DLR-IB 124-2004/31, Report of the Institute of Aerodynamics and Flow Technology, Braunschweig, ISSN 1614-7790, 2004.
28. Van Albada, G.D., Van Leer, B., and Roberts, W.W., "A Comparative Study of Computational Methods in Cosmic Gas Dynamics," *Astronomy and Astrophysics*, vol. 108, no. 1, 1982, pp. 76–84.
29. Nishikawa, H., and Liou, Y., "Third-Order Edge-Based Scheme for Unsteady Problems," AIAA-2018-4166, June 2018.
30. Salmon, J.T., Bogar, T.J., and Sajben, M, "Laser Doppler Velocimeter Measurements in Unsteady, Separated, Transonic Diffuser Flows," *AIAA Journal*, vol. 21, no. 12, 1983, pp. 1690–1697.
31. Eisfeld, B. and Rumsey, C., "Length-Scale Correction for Reynolds Stress Modeling," *AIAA Journal*, vol. 58, no. 4, 2020, pp. 1518–1528.